nature photonics

Article

https://doi.org/10.1038/s41566-023-01330-w

Determining the optimal communication channels of arbitrary optical systems using integrated photonic processors

Received: 29 May 2023

Accepted: 13 October 2023

Published online: 23 November 2023

Check for updates

SeyedMohammad SeyedinNavadeh[1], Maziyar Milanizadeh[1,6], Francesco Zanetto[1], Giorgio Ferrari[2], Marco Sampietro[1], Marc Sorel[3,4], David A. B. Miller[5], Andrea Melloni[1] & Francesco Morichetti[1]

Modes of propagation through an optical system are generally defined as the eigensolutions of the wave equation in the system. When propagation occurs through complicated or highly scattering media, however, modes are better identified as the best orthogonal communication channels to send information between sets of input and output apertures. Here we determine the optimal bidirectional orthogonal communication channels through arbitrary and scattering optical systems using photonic processors. The processors consist of meshes of electrically tuneable Mach–Zehnder interferometers in silicon photonics. The meshes can configure themselves based on simple power maximization or minimization algorithms, without external calculations or calibration or any prior knowledge of the optical system. The identification of the communication mode channels corresponds to a singular value decomposition of the entire optical system, autonomously performed by the photonic processors. We observe crosstalk below −30 dB between the optimized channels even in the presence of distorting masks or partial obstructions. In these cases, although the beams bear little resemblance to conventional mode families, they still show orthogonality. These findings offer potential for applications in multimode optical communication systems, promising efficient channel identification, adaptability to dynamic media and robustness against environmental challenges.

Finding the most efficient way to send information through a physical medium that is not well characterized, time varying or, in some cases, even completely unknown is a common problem in many different applications. Some examples include communications through turbulent systems[1,2] or multimode optical fibres[3], imaging through scattering media[4,5] or tissue[6], remote sensing[7], and beam shaping for localization and positioning[8]. In all these cases, information is carried by electromagnetic waves and the problem translates into identifying which waves can best propagate through the medium. Structural imperfections, material inhomogeneities and obstacles cause scattering and local distortions of the wavefront[9], resulting in deviations of the wave trajectory, end-to-end power loss and mixing or crosstalk among the waves or channels that co-propagate through the medium[10,11].

[1]Department of Electronics, Information and Bioengineering, Politecnico di Milano, Milan, Italy. [2]Department of Physics, Politecnico di Milano, Milan, Italy. [3]School of Engineering, University of Glasgow, Glasgow, UK. [4]TeCIP Institute, Scuola Superiore Sant'Anna, Pisa, Italy. [5]Ginzton Laboratory, Stanford University, Stanford, CA, USA. [6]Present address: Advanced Electronics and Photonics Research Centre, National Research Council Canada, Ottawa, Ontario, Canada. e-mail: francesco.morichetti@polimi.it

As shown by the generic scheme in Fig. 1a, any linear electromagnetic system with M input apertures and N output apertures can be described by an $N \times M$ matrix $\mathbf{M_c}$. This matrix depends on the optical properties of the medium and on the number and position of the apertures. The waves that experience the lowest end-to-end loss between these sets of apertures as well as not being subject to mutual mixing correspond to the 'communication modes' of the system[12,13]. If $\mathbf{M_c}$ is known a priori in some way, these eigensolutions can be readily obtained by calculating the singular value decomposition (SVD) of $\mathbf{M_c}$. SVD gives the set of orthogonal inputs that couple, one by one, to orthogonal outputs, giving independent communication channels. However, in many practical situations, $\mathbf{M_c}$ is not known; therefore, these solutions cannot be mathematically calculated.

In this work, we experimentally show that the best set of orthogonal waves that can propagate through arbitrary unknown optical media can be automatically found by using a pair of programmable photonic processors consisting of self-configuring meshes of Mach–Zehnder interferometers (MZIs), verifying a theoretical prediction of such a possibility[14]. MZI mesh architectures have been extensively used in previous works to 'synthesize' arbitrary non-unitary matrices by implementing on-chip SVD[15,16], with powerful demonstrations in computing systems based on photonic vector–matrix multiplication[17,18], photonic accelerators[19], cryptography[20], photonic neural networks[21–24], photonic analogue processors and equation solvers[25], and quantum photonic processors[26].

Here, instead, we use a pair of MZI architectures—one as a transmitter and another as a receiver—to 'analyse' an unknown medium and find the elements of its SVD factorization[14]; at the same time, this process physically sets up the orthogonal channels or communication modes, which are the best-coupled and lowest-crosstalk channels through the medium or optical system, independently of the medium or optical system.

Specifically, we use programmable meshes of integrated MZIs coupled to arrays of surface grating couplers (GCs), capable of generating[27,28], detecting[28,29] and spatially resolving[30] complex optical beams with arbitrary shapes. The computation of mesh settings for these waves is physically performed in situ by only using power minimization or maximization algorithms, without any need for the precalibration of mesh elements, any knowledge of the media or any external computation. We also show that the resulting vectors of input and output amplitudes experimentally correspond well to the theoretically optimal orthogonal SVD communication mode channels when the optical system is known and can be mathematically treated.

Results

Communication modes of an optical system

In the optical system (Fig. 1a), the 'left' and 'right' finite apertures define where the electromagnetic field is coupled and sampled, and they set discrete source and receiver vector spaces. The coupling between these sets of apertures can be described by a finite set of discrete bases consisting of M and N elements, respectively. Because of the beam divergence in an unconstrained volume, diffraction and scattering due to the presence of obstacles in the free-space path, and coupling loss between the optical beam and apertures, the matrix $\mathbf{M_c}_{[N\times M]}$ is generally non-unitary. Nonetheless, any matrix can be factorized according to the SVD as $\mathbf{M_c} = \mathbf{V\Sigma U}^{\dagger}$, where $\mathbf{U}_{[M\times M]}$ and $\mathbf{V}_{[N\times N]}$ are unitary matrices made from the left and right singular vectors $|\psi_{\mathbf{u}_m}\rangle$ and $|\phi_{\mathbf{v}_n}\rangle$, with $m = \{1,\ldots, M\}$ and $n = \{1,\ldots, N\}$ as their columns, respectively (Methods). The orthonormal basis sets $\{|\psi_{\mathbf{u}_m}\rangle\}_{m=1}^{M}$ and $\{|\phi_{\mathbf{v}_n}\rangle\}_{n=1}^{N}$ represent the 'communication mode pairs' of the system[12]. These orthogonal communication modes provide the field complex amplitudes, which maximize the power coupling between the source and receiving apertures, where the (power) coupling strengths associated with each mode pair are provided by the squared absolute value of the singular values $|\sigma_k|^2$, $k = \{1,\ldots, r = \mathrm{rank}\mathbf{M_c} \le \min(M, N)\}$.

To give an example, we first simulate the case of two identical sets of $M = N = 9$ optical apertures (sources and receivers), which are positioned on two parallel planes according to a 3×3 square array configuration. We assume that the spacing between the apertures of each array is about 32λ, where $\lambda = 1{,}550$ nm is the working optical wavelength, and that the two aperture planes are separated by a homogeneous medium (free space). The numerical solution to the SVD problem is shown in Fig. 1d for the first three modes with the highest coupling strengths. The different panels show the calculated far fields $\Psi_{\mathbf{u}_k}(\mathrm{el}, \mathrm{az})$, $k = \{1, 2, 3\}$ as a function of elevation (el) and azimuth (az) angles that are radiated by the left array of apertures when they are excited with the complex amplitudes of the left singular vectors $|\psi_{\mathbf{u}_k}\rangle$ (note that capital letters $\Psi_{\mathbf{u}_k}$ and $\Phi_{\mathbf{v}_k}$ are used to indicate the far fields of the left and right singular vectors, respectively). The normalized coupling strengths $|\sigma_k|^2$ for all the nine possible orthogonal communication modes are shown in a decreasing order (Fig. 1e). Note that the second and third communication modes are degenerate ($\Psi_{\mathbf{u}_2}$ and $\Psi_{\mathbf{u}_3}$ have the same shape, just rotated by 90°) with the same magnitude of their singular values $|\sigma_2| = |\sigma_3|$, providing the same coupling efficiency between the two aperture planes.

Experimental results

Now, we experimentally demonstrate that by using a pair of photonic integrated processors, these orthogonal modes can be automatically found. As shown in Fig. 1b, each processor consists of a mesh of tuneable MZIs that are connected to M and N optical apertures on the left- and right-hand side of the optical medium, respectively. The number of MZI diagonals, $\hat{M}$ and $\hat{N}$ for the left and right processor, respectively, identifies the number of modes the system can support and find, that is, $\min(\hat{M}, \hat{N})$. The two photonic processors used in this work are identical, with $\hat{M} = \hat{N} = 2$ (Fig. 1c), each diagonal enabling the processor to generate or collect a mode of the system[15]. Two integrated thermo-optic phase shifters independently set the relative phase shift between the two input waveguides and between the inner arms of each MZI, providing the desired functionality in the MZIs (Methods provides more details on the design and technology of the photonic chip). Two input ($I_{1,2}$)/output ($O_{1,2}$) waveguides are employed for coupling the light to standard single-mode optical fibres.

To automatically find the communication modes of the system, the MZI diagonal lines are controlled using a self-configuring algorithm aimed at maximizing the optical power at output ports O_1 and O_2 when light is injected at input ports I_1 and I_2, respectively[14,15,31]. Methods provides a step-by-step description of the operating procedure, and Supplementary Section 1 reports the mathematical treatment. Methods and Supplementary Section 2 describe the electronics employed to implement the automated control system. When the system converges to the final state, the cross-power coupling for $I_1 \to O_2$ and $I_2 \to O_1$ is minimized, meaning that the two orthogonal communication modes of the system are excited. In these conditions, the unitary processor on the left generates the best estimation of the first two left singular vectors $|\hat{\psi}_{\mathbf{u}_m}\rangle$, $m = \{1, 2\}$, and the processor on the right collects the first two right singular vectors $|\hat{\phi}_{\mathbf{v}_n}\rangle$, $n = \{1, 2\}$. Thus, the end-to-end transmission ($I_{1,2} \to O_{1,2}$) can be described by the following matrix (Methods):

$$\hat{\mathbf{\Sigma}} = \begin{bmatrix} \sigma_{11} & \sigma_{12} \\ \sigma_{21} & \sigma_{22} \end{bmatrix}, \quad (1)$$

where σ_{11} and σ_{22} are the estimated singular values of the first two eigenmodes (which are the most strongly coupled channels), whereas the off-diagonal terms σ_{12} and σ_{21} indicate any remaining crosstalk between these channels.

Figure 1f shows the measured far-field beam shapes $\Psi_{\hat{\mathbf{u}}_k}$, $k = \{1, 2, 3\}$ once the automated self-alignment of the two processors is completed.

https://doi.org/10.1038/s41566-023-01330-w

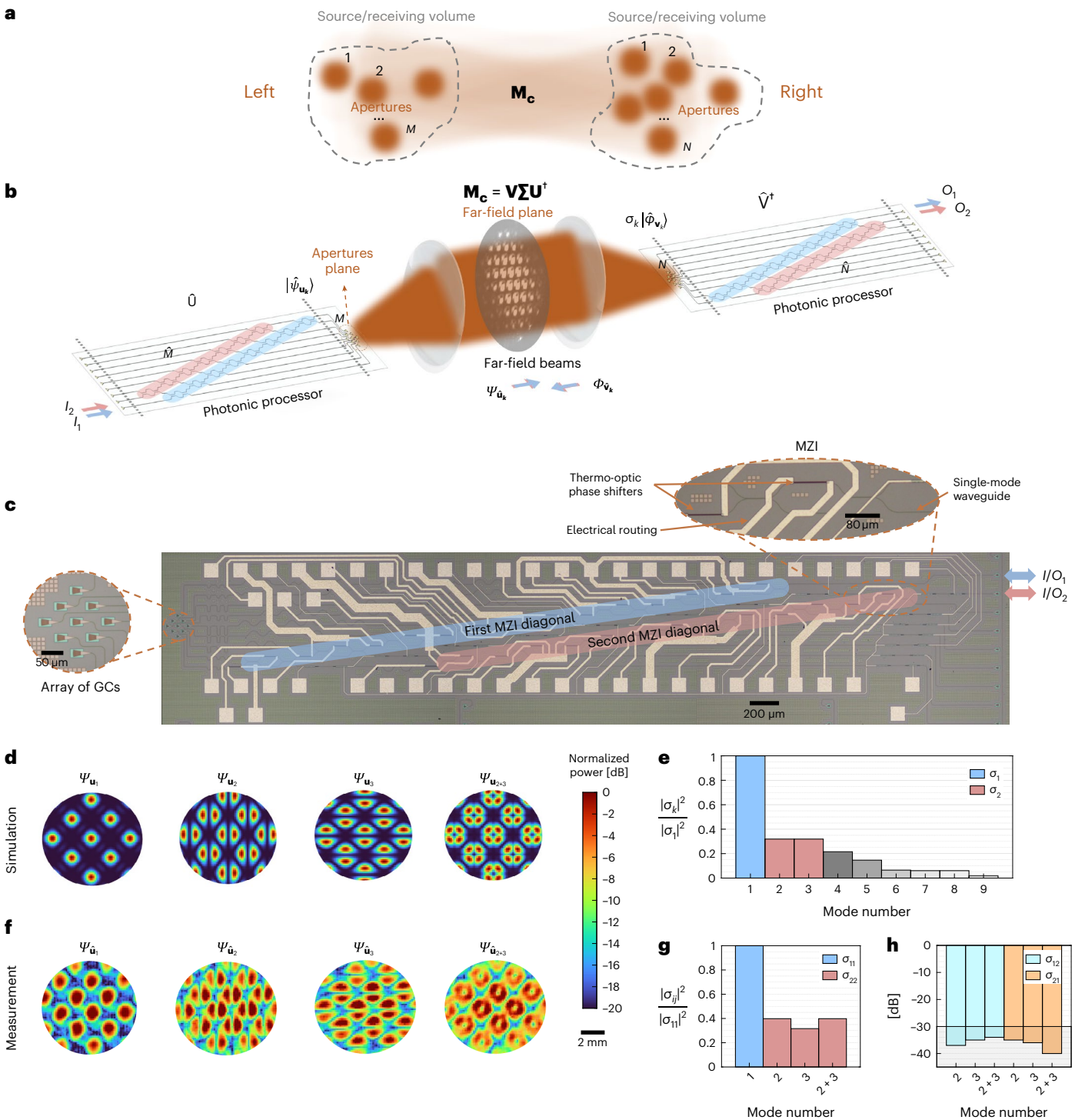

Fig. 1 | Automatically finding the best orthogonal communication modes with a pair of photonic integrated processors. a, Schematic of a generic optical system with M input and N output optical apertures in source and receiving volumes, respectively, which can be defined by a coupling matrix $\mathbf{M_c}$. **b**, Two programmable photonic integrated processors made of tuneable beamsplitters connected to M (left-hand side) and N (right-hand side) optical apertures are used to automatically find pairs of orthogonal communication modes through arbitrary optical media. $I_{1,2}$ and $O_{1,2}$ are the input and output ports of the processor, respectively, which define the end-to-end power coupling and crosstalk between two established channels. **c**, Top-view micro-photograph of the silicon photonic chip hosting nine optical apertures (3 × 3 square array of GCs) connected to a two-diagonal mesh of thermally tuneable MZIs. **d**,**f**, Far-field shapes of the first three modes that provide the highest coupling strengths between two symmetric sets of apertures ($M = N = 9$), as numerically obtained by computing the SVD of the system ($\Psi_{\mathbf{u}_k}$, $k = \{1, 2, 3\}$) (**d**) and experimentally obtained by finding them using a two-processor system ($\Psi_{\hat{\mathbf{u}}_k}$, $k = \{1, 2, 3\}$) (**f**). **e**,**g**, Simulation (all 9 modes; **e**) and experiment (first 2 modes; **g**) show the coupling strengths (σ_{ij}, $i = j$) normalized to the first mode. **h**, Orthogonality between the different communication modes (σ_{ij}, $i \neq j$) is experimentally demonstrated by the low cross-coupling (less than −30 dB). The error bar in the bar charts is about ±1.0 dB for optical crosstalk and less than 0.1 dB (about 2%) for the coupling strength.

https://doi.org/10.1038/s41566-023-01330-w

Both beam shapes and power-coupling strengths ($|\sigma_{ij}|^2$, $i=j$ (Fig. 1g)) agree very well with the results obtained from the SVD computation of the first two communication modes (Fig. 1d). Supplementary Fig. 1c shows a numerical simulation of the beam-shape evolution during the self-configuration of the two-mesh system, confirming the agreement of the experimental solutions found at convergence.

Interestingly, if the automated reconfiguration procedure of the two processors is restarted, the shape of the first eigenmode always converges to the Gaussian-like shape of $\Psi_{\hat{\mathbf{u}}_1}$, whereas the second strongly coupled mode may appear with the shape of $\Psi_{\hat{\mathbf{u}}_2}$ or $\Psi_{\hat{\mathbf{u}}_3}$ or with a combination of the two ($\Psi_{\hat{\mathbf{u}}_{2+3}}$) (Supplementary Video 1). This ambiguity is to be expected for degenerate eigenmodes. Nonetheless, as shown in Fig. 1g, the end-to-end coupled power in all these cases (pink bars) is almost the same, confirming the degeneracy of these two modes. Figure 1h shows that the cross-coupling between all the pairs of orthogonal eigenmodes is lower than −30 dB, that is, the off-diagonal terms of the $\hat{\mathbf{\Sigma}}$ matrix are negligible (Methods provides the loss analysis of the chip-to-chip system). This result confirms that the two-processor system automatically implements optical SVD in situ for the first two communications modes of the coupling matrix $\mathbf{M_c}$. Therefore, the left and right singular matrices $\mathbf{U}$ and $\mathbf{V}$, respectively, are correctly estimated by the two processors for these two communication modes and are embedded in the settings of the diagonal lines of MZIs.

Arbitrary sets of optical apertures. In the system considered so far, due to the symmetry of the left and right array apertures, the shapes of the first and second modes resemble (in each diffraction order) the shapes of the first and second Hermite–Gaussian (HG) modes. This property is not, however, maintained in situations with aperture arrays with arbitrary sizes or shapes on either side. Optimum orthogonal communication mode channels still exist in such cases, but we should have no expectation that such HG-like shapes are then associated with them.

In the case of left and right arrays with a different number of apertures, the coupling matrix $\mathbf{M_c}$ is no longer square ($M \neq N$). To experimentally emulate this condition, we used the same optical setup as shown in Fig. 1b, but we intentionally switched off selected subsets of apertures on both sides by 'freezing' an MZI in the chain in its 'bar' state, optically disconnecting any further MZIs from the processor (Fig. 2a). The automated configuration algorithm of the two-processor system is applied to control only the field radiated and received by the apertures that are operative. This means that in each considered case, the system is forced to use different discrete basis functions to describe the field at the aperture planes.

In the following, two different cases are considered: (1) Fig. 2b shows the case of a non-symmetric system where on one side, the number of 'ON' apertures in use is kept constant ($N=9$ on the right side) and on the other side, it is progressively reduced ($M=9, 8, \ldots, 4$); (2) Fig. 2c refers to a system with the same number of apertures in use ($M=N$) progressively reduced from 9 to 4 according to a (point-)symmetric configuration (Extended Data Fig. 1). The bar charts in both panels show the singular values σ_{11} (blue) and σ_{22} (pink) of the first two most strongly coupled modes (normalized to the reference case of $M=N=9$, leftmost bar) versus the number of apertures that are ON. In agreement with numerical simulations (Extended Data Fig. 2 shows a comparison with simulations), for both modes, although the coupling strength reduces with the number of OFF-state apertures, the coupling efficiency of the first mode remains about twice that of the second mode. In particular, however, in all the cases, the crosstalk between modes (given by σ_{12} (cyan) and σ_{21} (orange)) remains below −30 dB, confirming the mutual orthogonality of the established solutions.

The beam shapes for some example cases are shown in Fig. 2d. For the symmetric case of $M=N$, the same far-field shapes are obtained for the left $\Psi_{\hat{\mathbf{u}}_{1,2}}$ and right $\Phi_{\hat{\mathbf{v}}_{1,2}}$ modes, whereas for the non-symmetric case, $M \neq N$ different far-field shapes are observed since the left and right mode pairs are defined on different discrete spaces (Extended Data

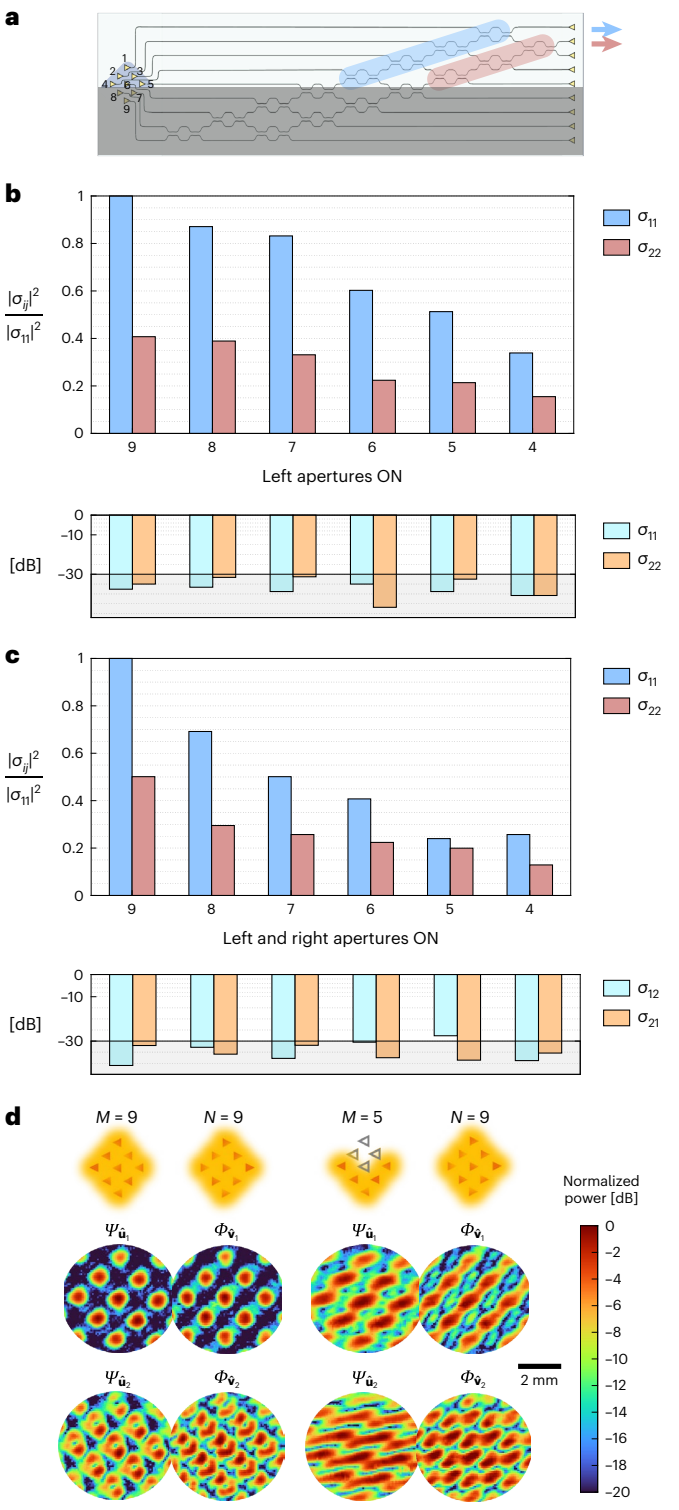

Fig. 2 | Orthogonal modes between arbitrary sets of optical apertures. **a**, Number of input M/output N optical apertures in the source/receiving volume can be modified by controlling the corresponding MZIs of the mesh processors. **b**,**c**, Measured input/output coupling strengths σ_{11} and σ_{22} of the first two modes (normalized to that of the first mode when $M=N=9$) when the number of apertures is reduced according to a non-symmetric ($M=9, 8, \ldots, 4$; $N=9$; **b**) or (point-)symmetric ($M=N=9, 8, \ldots, 4$; **c**) configuration. A high degree of orthogonality between the first two modes (crosstalk of less than −30 dB, as shown by σ_{12} and σ_{21} bars) is experimentally achieved in both cases (Extended Data Fig. 2 shows a comparison with simulations). **d**, Selected far-field beam shapes of the left and right modes for a symmetric case ($M=N=9$) and a non-symmetric case ($M=5, N=9$) (Extended Data Fig. 1 shows a complete set of beam shapes). The error bars are the same as those in Fig. 1.

https://doi.org/10.1038/s41566-023-01330-w

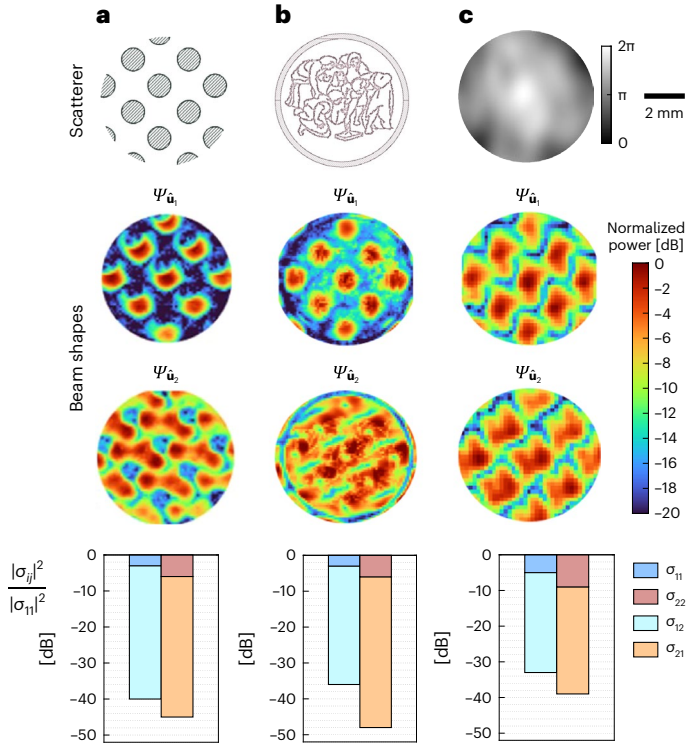

Fig. 3 | Orthogonal modes through obstacles and scattering media. **a**–**c**, Two-processor system is used to find pairs of orthogonal optical beams propagating through different kinds of obstacle. Periodic pattern of circular metal obstructions (**a**), microscale reproduction of the Politecnico di Milano logo (**b**) and phase-only aberrator (**c**). The far-field beam shapes providing the maximum coupling strengths and minimum mutual crosstalk are shown. The four bars represent σ_{ij}, $i,j = \{1, 2\}$, normalized to the power of the first mode without obstacle in the decibel scale, all starting from zero. For those scatterers with a periodic pattern, the periodicity of the scatterers matches the periodicity of the diffraction orders of the beam in the scatterer plane. The peak-to-peak phase shift introduced by the phase-only aberrator is 2π. The error bars are the same as those in Fig. 1.

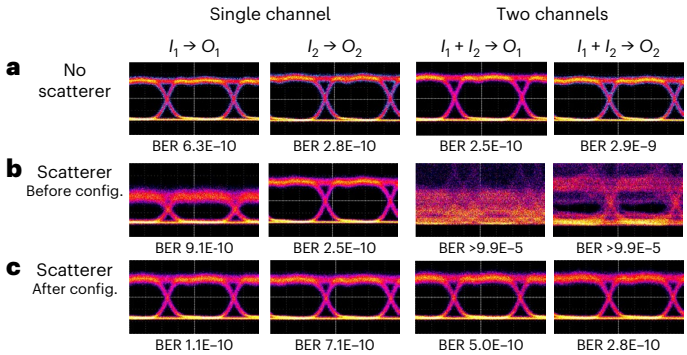

Fig. 4 | Orthogonality between data communication channels. **a**–**c**, Performances of a two-processor system are assessed by transmitting two intensity-modulated NRZ-OOK at 5 Gbps. **a**, Eye diagrams and BER of the reference channels that are individually transmitted (only a single channel is switched on) through the system in the absence of any obstacle; when the interfering channel is switched on (two channels), no substantial degradation is observed in the quality of the received signals. **b**, Insertion of an obstacle (specifically, a doughnut-like mask (Extended Data Fig. 3c) is used here) breaks the orthogonality between the communication modes causing strong channel interference and signal degradation. **c**, Reconfiguration of the two-processor system enables the establishment of a new pair of orthogonal modes that can be transmitted through the obstacle with negligible mutual crosstalk.

Fig. 1 shows a complete set of beam shapes). In any case, the reduction in the dimensionality of the aperture arrays breaks the original symmetry of the 3 × 3 square arrays and the best-coupled modes do not even approximately resemble any of the conventional families of modes typically considered in free-space optics (for example, HG, Laguerre–Gaussian and so on).

Beaming through obstacles. Theoretically, SVD predicts that orthogonal modes do always exist, irrespective of the coupling matrix $\mathbf{M_c}$ (ref. 12). This means that they can be found even in the presence of arbitrary obstacles or strongly scattering media between the aperture planes. To demonstrate this, we introduce different types of obstacle in the optical path (at the far-field plane; Fig. 1b) that partially obstruct and perturb the propagation of the optical field. Figure 3 shows a selection of obstacles, consisting of amplitude masks, which are patterned with the shape of periodic circular spots (Fig. 3a), where the period is the same as the diffraction orders in the far-field plane to maximize the impact, a non-periodic shape (Fig. 3b) and a phase-only aberrator emulated by using a spatial light modulator (Fig. 3c). After inserting the masks, the two processors self-configure to find the best end-to-end power couplings $I_1 \rightarrow O_1$ and $I_2 \rightarrow O_2$. As expected, the far-field shapes $\Psi_{\hat{\mathbf{u}}_1}$ and $\Psi_{\hat{\mathbf{u}}_2}$ that result after the processors establish the best chip-to-chip communication through different obstacles do not correspond to any standard mode sets (for example, HG), yet they are still mutually orthogonal. The orthogonality between these modes is confirmed by the very low crosstalk (σ_{ij}, $i \neq j$) shown in the bar charts in Fig. 3, and the singular values (σ_{ij}, $i = j$) are only slightly reduced with respect to the reference case (no mask). Extended Data Fig. 3 shows other cases with different mask shapes and corresponding beam shapes and crosstalks between orthogonal channels.

Data communication experiment. The two-processor system was employed to perform a data communication experiment between the two chips. Figure 4 shows the eye diagrams and the bit error ratio (BER) of two intensity-modulated non-return-to-zero (NRZ) on–off-keying (OOK) signals at a data rate of 5 Gbps, which are injected at input ports I_1 and I_2 of the first chip and extracted at output ports O_1 and O_2 of the second chip. The quality of the signals simultaneously transmitted by using the modes determined by the processors (Fig. 4a, two channels) is comparable with the quality of the signals that are individually transmitted (Fig. 4a, single channel). The presence of an obstacle breaks such orthogonality, introducing mutual optical crosstalk and deteriorating the transmission performance (Fig. 4b); however, the two-processor system can find the pair of optimal communication channels that remain orthogonal through such an obstacle, recovering the reference BER performance (Fig. 4c).

Discussion

We demonstrated the automatic finding of orthogonal communication modes between arbitrary sets of optical apertures at both ends of a free-space optical system. The effective computation of these modes is physically performed through a pair of programmable photonic processors made of self-configuring MZIs, without any knowledge of the optical system in between and without any need for the calibration of processor elements. Essentially, no crosstalk between mode pairs (experimentally better than −30 dB) is obtained even when the number and configuration of optical apertures at the two ends are different, and even when amplitude obstructions and/or phase perturbations are introduced in the free-space medium.

In all cases that can also be readily simulated, these beams experimentally correspond well to the theoretical optimal orthogonal communication mode channels, which can be mathematically calculated using SVD. Especially in cases with obstructions or different aperture sets on the two ends, these optimal modes may have little or no

similarity to standard mode families; nonetheless, they show low cross-talk associated with orthogonality. Mathematically, only these SVD channels or communication modes maximize the power transmission and are orthogonal[12].

In this work, these concepts are experimentally validated by using photonic processors with two diagonal lines of MZIs connected to nine input/output integrated apertures (square arrays of GCs), which are used to find the first two orthogonal modes of several different free-space optical systems; however, this approach is scalable to more than two modes by using mesh architectures with a larger number of optical inputs and outputs and more MZI diagonal lines[18] (Methods). Once the optical apertures in the source and receiving volumes are set, all the communication modes between them are sequentially found, starting from the one with the strongest singular value (best-coupled mode) down to the ones with progressively lower singular values (less strongly coupled modes). Modes with closely spaced singular values (that is, quasi-degenerate modes) are more sensitive to any perturbation of the system. Therefore, the order according to which quasi-degenerate modes are found can be modified by small changes in the system, and this is what actually happens to modes $\Psi_{\hat{\mathbf{u}}_2}$ and $\Psi_{\hat{\mathbf{u}}_3}$ in the experiment (Fig. 1f). Nonetheless, the modes that are found are always guaranteed to be orthogonal, and they represent the two most strongly coupled modes in each case.

Within the operational wavelength range of the two-processor system (Methods), multiple wavelength-division multiplexed channels can be mapped onto the same communication mode. This means that wavelength can be used as another basis for scaling the number of channels, provided that the entire optical system (including obstacles, aberrators and so on) equally affects all the wavelengths. Further, each mode can be individually established and adaptively optimized (for instance, in dynamically varying media) without the need for switching off the other coexisting modes, provided that each transmitted beam is labelled with a suitable pilot tone (Supplementary Section 2)[32].

Although the examples reported in this work refer only to forward-propagating modes, once the free-space optical system is set (that is, the number and position of the input/output apertures and the presence/absence of obstacles in between), due to the reciprocity of the system, the same mode pairs are established for forward and backward propagation. Also, the presented results can be straightforwardly generalized to the case of chips that do not remain fixed in space, because the two-processor system allows us also to send and receive optical beams along different directions[27,29].

The proposed system could also be used to find the guided modes in a multimode optical fibre that exhibit the highest end-to-end mutual isolation even in the presence of bending, deformation and structural defects[3]. Since photonic processors preserve the phase information encoded in the optical signals, our approach even applies to coherent transmission systems with arbitrary amplitude- and phase-modulation formats as well as to spatial-division multiplexing systems to handle signal orthogonalization directly in the optical domain[33], and does not require any digital signal processing at the data rate to make such orthogonalization. Finally, the reconfiguration time of photonic processors realized on a silicon photonic platform, which is faster than 10 μs in the case of thermal actuators[34] and in the sub-nanosecond range for electro-optic actuators[35], should also allow real-time adaptation[36] of the optimal modes to time-varying media, such as turbulent environments, potentially as fast as or faster than available wavefront shapers[37].

Online content

Any methods, additional references, Nature Portfolio reporting summaries, source data, extended data, supplementary information, acknowledgements, peer review information; details of author contributions and competing interests; and statements of data and code availability are available at https://doi.org/10.1038/s41566-023-01330-w.

References

1. Cox, M. A. et al. Structured light in turbulence. *IEEE J. Sel. Topics Quantum Electron.* **27**, 1–21 (2021).
2. Hill, R. J. Optical propagation in turbulent water. *J. Opt. Soc. Am.* **68**, 1067–1072 (1978).
3. Matthès, M. W., Bromberg, Y., de Rosny, J. & Popoff, S. M. Learning and avoiding disorder in multimode fibers. *Phys. Rev. X* **11**, 021060 (2021).
4. Vellekoop, I. M. & Mosk, A. P. Focusing coherent light through opaque strongly scattering media. *Opt. Lett.* **32**, 2309–2311 (2007).
5. Yoon, S. et al. Deep optical imaging within complex scattering media. *Nat. Rev. Phys.* **2**, 141–158 (2020).
6. Biton, N., Kupferman, J. & Arnon, S. OAM light propagation through tissue. *Sci. Rep.* **11**, 2407 (2021).
7. Ishimaru, A. The beam wave case and remote sensing. in *Laser Beam Propagation in the Atmosphere. Topics in Applied Physics* (ed Strohbehn, J. W.) 129–170 (Springer, 1978).
8. Heck, M. J. R. Highly integrated optical phased arrays: photonic integrated circuits for optical beam shaping and beam steering. *Nanophotonics* **6**, 93–107 (2017).
9. Nape, I. et al. Revealing the invariance of vectorial structured light in complex media. *Nat. Photon.* **16**, 538–546 (2022).
10. Churnside, J. H. & Lataitis, R. J. Wander of an optical beam in the turbulent atmosphere. *Appl. Opt.* **29**, 926–930 (1990).
11. Gong, L. et al. Optical orbital-angular-momentum-multiplexed data transmission under high scattering. *Light Sci. Appl.* **8**, 27 (2019).
12. Miller, D. A. B. Waves, modes, communications, and optics: a tutorial. *Adv. Opt. Photon.* **11**, 679–825 (2019).
13. Miller, D. A. B. Communicating with waves between volumes: evaluating orthogonal spatial channels and limits on coupling strengths. *Appl. Opt.* **39**, 1681–1699 (2000).
14. Miller, D. A. B. Establishing optimal wave communication channels automatically. *J. Lightwave Technol.* **31**, 3987–3994 (2013).
15. Miller, D. A. B. Self-configuring universal linear optical component. *Photon. Res.* **1**, 1–15 (2013).
16. Harris, N. C. et al. Linear programmable nanophotonic processors. *Optica* **5**, 1623–1631 (2018).
17. Zhou, H. et al. Chip-scale optical matrix computation for PageRank algorithm. *IEEE J. Sel. Topics Quantum Electron.* **26**, 8300910 (2020).
18. Bogaerts, W. et al. Programmable photonic circuits. *Nature* **586**, 207–216 (2020).
19. Zhou, H. et al. Photonic matrix multiplication lights up photonic accelerator and beyond. *Light Sci. Appl.* **11**, 30 (2022).
20. Pai, S. et al. Experimental evaluation of digitally verifiable photonic computing for blockchain and cryptocurrency. *Optica* **10**, 552–560 (2023).
21. Shen, Y. et al. Deep learning with coherent nanophotonic circuits. *Nat. Photon.* **11**, 441–446 (2017).
22. Shokraneh, F., Geoffroy-gagnon, S. & Liboiron-Ladouceur, O. The diamond mesh, a phase-error- and loss-tolerant field-programmable MZI-based optical processor for optical neural networks. *Opt. Express* **28**, 23495–23508 (2020).
23. Tian, Y. et al. Scalable and compact photonic neural chip with low learning-capability-loss. *Nanophotonics* **11**, 329–344 (2022).
24. Pai, S. et al. Experimentally realized in situ backpropagation for deep learning in photonic neural networks. *Science* **380**, 398–404 (2023).
25. Tzarouchis, D. C., Mencagli, M. J., Edwards, B. & Engheta, N. Mathematical operations and equation solving with reconfigurable metadevices. *Light Sci. Appl.* **11**, 263 (2022).

26. Harris, N. C. et al. Quantum transport simulations in a programmable nanophotonic processor. *Nat. Photon.* **11**, 447–452 (2017).
27. Milanizadeh, M. et al. Coherent self-control of free-space optical beams with integrated silicon photonic meshes. *Photon. Res.* **9**, 2196–2204 (2021).
28. Miller, D. A. B. Analyzing and generating multimode optical fields using self-configuring networks. *Optica* **7**, 794–801 (2020).
29. Milanizadeh, M. et al. Separating arbitrary free-space beams with an integrated photonic processor. *Light Sci. Appl.* **11**, 197 (2022).
30. Bütow, J. et al. Spatially resolving amplitude and phase of light with a reconfigurable photonic integrated circuit. *Optica* **9**, 939–946 (2022).
31. Miller, D. A. B. Self-aligning universal beam coupler. *Opt. Express* **21**, 6360–6370 (2013).
32. Annoni, A. et al. Unscrambling light-automatically undoing strong mixing between modes. *Light Sci. Appl.* **6**, 17110–17110 (2017).
33. Fontaine, N. K. et al. Space-division multiplexing and all-optical MIMO demultiplexing using a photonic integrated circuit. In *National Fiber Optic Engineers Conference* PDP5B.1 (Optica Publishing Group, 2012).
34. Harris, N. C. et al. Efficient, compact and low loss thermo-optic phase shifter in silicon. *Opt. Express* **22**, 10487–10493 (2014).
35. Rahim, A. et al. Taking silicon photonics modulators to a higher performance level: state-of-the-art and a review of new technologies. *Adv. Photon.* **3**, 024003 (2021).
36. Choutagunta, K., Roberts, I., Miller, D. A. B. & Kahn, J. M. Adapting Mach-Zehnder mesh equalizers in direct-detection mode-division-multiplexed links. *J. Lightwave Technol.* **38**, 723–735 (2020).
37. Tzang, O. et al. Wavefront shaping in complex media with a 350 kHz modulator via a 1D-to-2D transform. *Nat. Photon.* **13**, 788–793 (2019).

Methods

SVD factorization of the optical system

In this section, we define the main parameters of the SVD factorization of the optical system we are considering. According to SVD theory, any matrix can be factorized as

$$\mathbf{M_c} = \mathbf{V\Sigma U}^{\dagger} = \begin{bmatrix} | & & | \\ |\phi_{\mathbf{v}_1}\rangle & \dots & |\phi_{\mathbf{v}_N}\rangle \\ | & & | \end{bmatrix} \begin{bmatrix} \sigma_1 & & & \\ & \ddots & & 0 \\ & & \sigma_r & \\ & 0 & & \end{bmatrix} \begin{bmatrix} - & \langle\psi_{\mathbf{u}_1}| & - \\ & \vdots & \\ - & \langle\psi_{\mathbf{u}_M}| & - \end{bmatrix} \quad (2)$$

where the dagger † indicates a Hermitian adjoint or conjugate transpose (in this 'Dirac' notation, $\langle\alpha|$, which can be viewed as a 'row' vector, is the Hermitian adjoint of the 'column' vector $|\alpha\rangle$). $\mathbf{U}_{[M\times M]}$ and $\mathbf{V}_{[N\times N]}$ are unitary matrices made from the left and right singular vectors as

$$|\psi_{\mathbf{u}_m}\rangle = \begin{bmatrix} u_{1m} \\ \vdots \\ u_{Mm} \end{bmatrix}, \quad |\phi_{\mathbf{v}_n}\rangle = \begin{bmatrix} v_{1n} \\ \vdots \\ v_{Nn} \end{bmatrix}, \quad (3)$$

with $m = \{1, \dots, M\}$ and $n = \{1, \dots, N\}$ as their columns, respectively, and $\mathbf{\Sigma}_{[N\times M]}$ is a diagonal matrix with singular values σ_k, $k = \{1, \dots, r = \text{rank}\mathbf{M_c} \leq \min(M, N)\}$, arranged in the descending order according to the magnitudes ($|\sigma_1| \geq |\sigma_2| \geq \dots \geq |\sigma_r| > 0$) of its non-zero elements. Note that the choice of 'left' and 'right' is according to the schematic of the two sets of apertures shown in Fig. 1a, which is the opposite of the mathematical notation often used with SVD. The inputs $|\psi_{\mathbf{u}_k}\rangle$ and outputs $\sigma_k|\phi_{\mathbf{v}_k}\rangle$ are uniquely specified (at least within the normalization and phase factors, and arbitrariness of degenerate solutions), and the orthonormal basis sets $\{|\psi_{\mathbf{u}_m}\rangle\}_{m=1}^{M}$ and $\{|\phi_{\mathbf{v}_n}\rangle\}_{n=1}^{N}$ represent the 'communication mode pairs' of the system[12].

The sets of orthogonal input vectors $|\psi_{\mathbf{u}_k}\rangle$ that couple in a one-by-one manner to orthogonal output vectors $|\phi_{\mathbf{v}_k}\rangle$, with coupling strengths σ_k, always exist for any matrix, and hence, such orthogonal channels always exist, regardless of the linear medium or optics between the inputs and outputs[12,13]. Note too that, in the communication modes approach[12], it is the pairs of vectors $|\psi_{\mathbf{u}_k}\rangle$ and $|\phi_{\mathbf{v}_k}\rangle$ that are the 'modes' in the system. Each of these vectors is a solution of an eigenproblem; $|\psi_{\mathbf{u}_k}\rangle$ is an eigenvector of $\mathbf{M_c^{\dagger}M_c}$ and $|\phi_{\mathbf{v}_k}\rangle$, of $\mathbf{M_cM_c^{\dagger}}$ (with relation $\mathbf{M_c}|\psi_{\mathbf{u}_k}\rangle = \sigma_k|\phi_{\mathbf{v}_k}\rangle$). The electromagnetic field or beam between the inputs and outputs is not itself the mode and is not the solution of an eigenproblem, and—unlike many common families of 'modes'—it does not necessarily retain its shape as it propagates[12].

Due to the symmetry of this specific system, the backward singular vectors $|\phi_{\mathbf{v}_k}\rangle$ from the right array of apertures would be the complex conjugates (phase conjugates) of $|\psi_{\mathbf{u}_k}\rangle$, and therefore would have the same power far-field shapes.

The two-processor system is used to estimate the singular value matrix $\mathbf{\Sigma}$ as

$$\hat{\mathbf{\Sigma}}_{[\hat{N}\times\hat{M}]} = \hat{\mathbf{V}}^{\dagger}_{[\hat{N}\times N]}(\mathbf{V\Sigma U}^{\dagger})_{[N\times M]}\hat{\mathbf{U}}_{[M\times\hat{M}]}, \quad (4)$$

where the processor on the left generates the best estimation of the left singular vectors $|\hat{\psi}_{\mathbf{u}_m}\rangle, m = \{1, \dots, \hat{M} \leq M\}$, which are the columns of $\hat{\mathbf{U}}$, and the processor on the right generates the right singular vectors $|\hat{\phi}_{\mathbf{v}_n}\rangle, n = \{1, \dots, \hat{N} \leq N\}$, which are the columns of $\hat{\mathbf{V}}$. The 'hat' in the notation is used to indicate parameters that are estimated by the two-processor system. The consistency of our numerical and experimental results and their agreement with what we expect from SVD modelling (as well as fundamental theory) are strong evidence that the two-processor system finds a very good approximation to the ideal SVD channels (or communication modes).

Mode orthogonality is evaluated by measuring the end-to-end crosstalk, which is given by the ratio between the cross-coupling between different modes (off-diagonal terms $|\sigma_{ij}|^2$ of $\hat{\mathbf{\Sigma}}$, with $i \neq j$) and the power of the considered mode (diagonal terms $|\sigma_{ij}|^2$, with $i = j$).

Configuration algorithm

To understand how this system works, consider the architecture shown in Fig. 1b. Each photonic processor consists of two diagonal lines of MZIs. Suppose first we shine light into the upper waveguide I_1 on the left and hence into the 'first' (blue) diagonal line of MZIs in this processor. For the moment, we presume that the phase shifters in the MZIs are set in some arbitrary way. As a result, generally, some light will appear out of each of the nine waveguides on the right side of this left photonic processor. This light emerges from the gratings and passes into the optical system (characterized by some matrix $\mathbf{M_c}$). Some resulting light is then collected by the gratings at the inputs to the right photonic processor, and passes into the first (blue) diagonal line of MZIs in the right processor.

A key point is that this 'blue' diagonal line in the photonic processor on the right can now function as a self-aligning beam coupler[31]. A simple progressive algorithm allows us to set all the MZIs in this diagonal line so that all the input power in all the nine waveguides is routed to the output waveguide O_1 at the upper right. Such an algorithm can work by progressively configuring each MZI, starting with the one at the bottom left of this row, so that no power from it passes into the second (pink) row; equivalently all the power in this MZI is routed to its upper output. We can then proceed similarly along the diagonal row of MZIs, so all the power ends up in output waveguide O_1. We can run this algorithm based on signals from mostly transparent photodetectors (PDs) in the waveguides between the blue and pink rows[32], successively minimizing the powers in them, or we can run a version of this algorithm based only on maximizing the power in output O_1 (ref. 31). The second option was used in the experiments reported in this work. In particular, a dithering-based strategy was implemented to enable the simultaneous monitoring and control of several MZIs with a single external PD (see the 'Control electronics' section).

This first self-aligning process has successfully coupled all the power collected by gratings on the right to output O_1, but it has not yet established the overall optimum channel through the whole system. To find this channel, we can proceed next by turning off the input power at port I_1, and instead shining power backward into O_1. Then, we similarly self-align the MZIs in the first (blue) line of MZIs in the left photonic processor to couple all this collected backward power into waveguide I_1. If we then alternately repeat this process forward and backward, the whole system will converge to the best-coupled channel, as mathematically shown in another work[14] (Supplementary Section 1). This process has, therefore, found the first, most strongly coupled communication mode of the entire system, essentially by a variational process.

Now, if we shine input power into the second waveguide I_2 in the left photonic processor, and hence into the second (pink) line of MZIs, this power will emerge from the gratings in that left processor, and some of it will be coupled through the optical system and the gratings in the right processor and into the waveguides and MZI lines in that processor. A key point is that because we have set the 'blue' lines of MZIs to implement the first communication mode, none of that power originally shone into I_2 will emerge from the upper waveguide O_1. This is guaranteed by the orthogonality of the communications modes and the unitarity of the processors (where we note that unitary processors preserve orthogonalities). Any input fields to the optical system that are orthogonal to the first communication mode's input field will generate output fields that are orthogonal to the first communication mode's output field. Instead, all the input power at port I_2 will flow into the second (pink) line of MZIs in the right photonic processor.

We can then repeat the same kind of backward and forward process with these second (pink) lines of MZIs and their associated waveguides I_2 and O_2. This process will converge these second lines to find and

implement the second-most strongly coupled communications mode. If we had more diagonal lines in the processors, we could continue this process to establish successive communication modes.

The forward-and-backward algorithm described above was used to configure the two-processor system in the experiments (Figs. 1 and 2). When performing these experiments, we realized that actually a forward-only propagation algorithm worked as well, providing convergence of the system to the same final state. In the forward-only algorithm, the light is shown only in one direction and all the MZIs of the same line of the left and right processors are set at the same time. For instance, to establish the first communication mode, light is injected from input I_1 and the 32 phase shifters of the first (blue) diagonal lines of MZIs are simultaneously driven to maximize the power at the output port O_1. Once the first communication channel is optimized, the procedure is repeated for the second channel (second pink diagonal lines of the MZI). The main advantage of the forward-only algorithm is that it requires neither light sources at the receiver side nor multiple iterations, so it makes the configuration more practical without affecting the degree of mode orthogonality with respect to the forward-and-backward algorithm (at least in all the examples considered in this work). Results reported in Fig. 3 and Extended Data Fig. 3 were obtained with the forward-only algorithm.

Control electronics

The control strategy employed for the automated self-configuration of the photonic processors is based on the implementation of local feedback loops that individually monitor and stabilize each MZI tuneable coupler[15]. To this end, dithering signals are applied to the thermo-optic phase shifters to identify the deviation from the optimum bias point[38] and maximize the optical power detected at an external PD coupled at the output port of the photonic chips. The external PD used in our experiment offers better sensitivity (about −55 dBm) than the standard integrated PDs available from the silicon foundry (about −35 dBm). Such an external PD allows to detect weaker light signals, as required, when the automated configuration of the system starts from arbitrary conditions of the two processors and the coupling loss can be as high as 70 dB (Supplementary Section 3). High-sensitivity integrated PDs would be more suitable for real applications and could provide an interesting solution for future implementations[39]. The electronic controller of the two-chip photonic system (counting 30 MZIs and 60 thermal phase shifters) is made of four customized motherboards, hosting 16 parallel lock-in chains each with phase shifter drivers and readout stages for the extraction of the error signal (Supplementary Fig. 2a). Different pairs of orthogonal frequencies, ranging from 6.1 to 47.6 kHz, are employed for the two phase shifters of each MZI. The electrical bandwidth of the feedback loop controller is limited by the frequency spacing between the dithering frequencies, thus resulting in a stabilization time of about 50 ms for each MZI line. The digital control electronics operate with 12 bits, meaning an accuracy of about 1 mV as the control voltage on the thermal tuners is in the worst condition (5 V). This corresponds to a phase uncertainty of the phase shift induced by the thermal tuners of about 1 mrad, which—in an ideal MZI—would lead to a negligible crosstalk of about −60 dB per MZI. Supplementary Section 2 provides more details on the control electronics.

Photonic processor design and main building blocks

The integrated photonic processors are fabricated on a standard 220 nm silicon photonics platform (Advanced Micro Foundry) and are designed for operation in the 1,550 nm wavelength range. The photonic chip size is 5.8 mm × 1.3 mm. Supplementary Fig. 4 summarizes the main characteristics of the photonic building blocks used in the photonic processors. All the waveguides are single-mode channel waveguides with 500 nm width and a propagation loss of about 1 dB cm^{-1}. The on-chip array of apertures is implemented by means of a 3 × 3 square array of surface GCs that couple the light into/from free space (Fig. 1c). The nine GCs of the two-dimensional (2D) array are standard building blocks of the silicon photonics platform; no specific optimization of the GC design was carried out because the applications presented in this work apply to any kind of optical aperture. The centre-to-centre spacing of the GCs is 50 μm ≈ 32λ, such spacing being constrained by the size of each GC (29.2 μm × 19.3 μm) and by the waveguide bundle required for routing the light from each GC to the input ports of the MZI processor. The periodicity in the far-field pattern (diffraction orders) is a consequence of the large spacing ($\gg \frac{\lambda}{2}$) between the array elements, which leads to multiple diffraction 'replicas' of the underlying mode shapes. Such a spacing is not a critical issue, because the presented results apply to any arbitrary spacing between apertures and also to randomly positioned apertures (a non-periodic grid). For specific applications where grating lobes need to be mitigated, GCs with a smaller footprint can be designed to reduce the mutual spacing[40] and double-layer photonic platforms, such as silicon nitride on silicon[41], can be used to enable a more packed routing of the output waveguide array.

Each GC emits/receives transverse-electric-polarized light within a radiation angle of 5° × 9° centred around a 12°-tilted direction with respect to the normal to the chip surface. The 2D array has an overall beamwidth of 0.6° × 0.6°, which is a field of view of about 1.7°. To experimentally observe the far field emitted by the two photonic chips, a 4f lens system is used, so that the plane of the apertures is Fourier transformed and collimated at a resulting Fourier plane between the two lenses, that is, the far-field plane (Fig. 1b). Far-field measurements are performed with an infrared camera that images this Fourier plane (Supplementary Section 3 provides more details on the experimental setup).

The MZIs have 3 dB directional couplers with 300 nm gap spacing between the coupled waveguides and 40 μm length of the coupling region. Phase shifters are realized through TiN thermal tuners (80 μm × 2 μm) deposited on top of the oxide above the waveguide, at a distance of 2 μm above the silicon waveguide core. The thermal tuners have a power efficiency of 22 mW π^{-1} and a time response of about 10 μs. To mitigate thermal crosstalk issues, a thermal crosstalk cancellation technique[42] is used to improve the efficiency of the control algorithm. The power consumption for the full configuration of the two-processor system, including 30 phase shifters per chip, is about 1.3 W in the worst case where a 2π phase shift would have to be applied to all the thermal tuners of the processor. Scalability of the system to larger-scale circuits would benefit from the use of non-thermal actuators, exploiting materials with high electro-optic coefficients such as lithium niobate or barium titanate integrated in silicon waveguides, or opto-micromechanical phase shifters.

Loss analysis and wavelength dependence

Here we analyse the optical power budget for the free-space setup used in our experiments. The mesh processors do not introduce any fundamental loss for splitting or combining the beams, since they ideally implement unitary linear transformations. An overall on-chip loss of about 2 dB is observed, which is due to propagation loss of the waveguides (<1.00 dB), bending loss and the excess loss of the directional couplers (<0.05 dB each) of the MZIs. The coupling loss between the GCs and in/out single-mode fibres is 4.5 dB per optical input/output. A 50:50 beamsplitter (3 dB loss) is added in the free-space optics for monitoring the beam shapes with the near-infrared camera at the far-field plane and an additional 3 dB loss is due to the aberration of the optical system and possible minor alignment tolerances in the experimental setup (Supplementary Section 3). For the first-order mode, the end-to-end loss of the entire system in the absence of obstacles is about 35 dB, meaning that the coupling loss between the free-space mode and 2D arrays is about 8 dB per array. Such loss can be substantially reduced by improving the fill factor of the 2D array or by using

off-chip focusing/collimating optics, such as lenslet arrays in front of the GCs and/or telescopes; nonetheless, since SVD applies to generic non-unitary matrices, the orthogonality of the established modes is always preserved even in highly lossy systems and through strongly diffractive/scattering media.

The GCs are connected to the photonic processor through optical waveguides with the same optical length to minimize the wavelength dependence of the entire circuit[29]. The wavelength range across which the photonic processors can operate is about 35 nm (from 1,535 to 1,570 nm)[29], this wavelength range is mainly limited by the wavelength-selective response of the GCs and by the wavelength dependence of the 3 dB directional couplers of the MZIs. Such wavelength dependence can be reduced by using optimized designs for broadband GCs[43] and for broadband directional couplers[44].

Scalability to larger optical systems

The effective number of available modes is associated with the non-zero singular values of the coupling matrix—that is, with the rank of $\mathbf{M_c}$ (ref. 12)—which is at most $\min(M, N)$. Each additional aperture (on both processors) can potentially increase the number of available channels. In the system with 3 × 3 apertures, up to nine orthogonal modes exist, whose singular values are shown in Extended Data Fig. 2 (evidently, by reducing the number of gratings, the available number of modes decreases accordingly). Among them, the number of modes that can be found by the two-processor system is $\min(\hat{M}, \hat{N})$. The number of required MZI lines, namely, $\hat{M}$ and $\hat{N}$, scales linearly with the number of modes to be found. Therefore, a system with 9 × 9 apertures (on both input/output sides $M = N = 81$) would need up to $M - 1 = 80$ MZI lines per processor to find all the modes, corresponding to $M(M-1)/2 = 3{,}240$ MZIs.

By increasing the number of optical apertures and keeping the same pitch, the coupling strengths (that is, the singular values) of all the modes increase (Extended Data Fig. 2). This result is in line with the theory of phased-array antenna systems, where by increasing the number of elements, the gain of the radiation pattern increases and the beam divergence reduces.

The extension of the approach to the case of chips that do not remain fixed in space does not lead to an increase in the complexity of either the photonic circuits or the configuration algorithm. In fact, each MZI of the transmitter (receiver) integrates an output (input) thermal tuner (Supplementary Fig. 2) that is used to adjust the relative phase of the optical fields in the waveguide array. These phase shifters can be also used to provide the additional phase tilt that is required for scanning the beam, as happens in a light detection and ranging system[45]. As a result, pairs of orthogonal beams can be always found irrespective of the direction of arrival, because any coupling matrix $\mathbf{M_c}$ can be decomposed according to SVD, and the two-processor system self-configures in the same way as in the case of fixed chips, regardless of the direction of the beams.

Data availability

All the data supporting the findings of this study are available within this Article and its Supplementary Information. Any additional data are available from the corresponding author on reasonable request.

Code availability

The computer codes that support the plots within this paper and other findings of this study are available from the corresponding author upon reasonable request.

References

38. Zanetto, F. et al. Dithering-based real-time control of cascaded silicon photonic devices by means of non-invasive detectors. *IET Optoelectronics* **15**, 111–120 (2021).
39. Xue, Y. et al. High-speed and low dark current silicon-waveguide-coupled III-V photodetectors selectively grown on SoI. *Optica* **9**, 1219–1226 (2022).
40. Fatemi, R., Khial, P. P., Khachaturian, A. & Hajimiri, A. Breaking FOV-aperture trade-off with multi-mode nano-photonic antennas. *IEEE J. Sel. Topics Quantum Electron.* **27**, 6100614 (2021).
41. Sacher, W. D., Huang, Y., Lo, G.-Q. & Poon, J. K. S. Multilayer silicon nitride-on-silicon integrated photonic platforms and devices. *J. Lightwave Technol.* **33**, 901–910 (2015).
42. Milanizadeh, M., Aguiar, D., Melloni, A. & Morichetti, F. Canceling thermal cross-talk effects in photonic integrated circuits. *J. Lightwave Technol.* **37**, 1325–1332 (2019).
43. Zemtsov, D. S. et al. Broadband silicon grating couplers with high efficiency and a robust design. *Opt. Lett.* **47**, 3339–3342 (2022).
44. Lu, Z. et al. Broadband silicon photonic directional coupler using asymmetric-waveguide based phase control. *Opt. Express* **23**, 3795–3808 (2015).
45. Poulton, C. V. et al. Long-range LiDAR and free-space data communication with high-performance optical phased arrays. *IEEE J. Sel. Topics Quantum Electron.* **25**, 7700108 (2019).

Acknowledgements

S.S., G.F., M. Sampietro, M. Sorel, A.M. and F.M. acknowledge support from the European Commission under the Horizon 2020 Programme (SuperPixels, grant no. 829116). S.S., M. Sorel, A.M. and F.M. acknowledge support from the Italian National Recovery and Resilience Plan (NRRP) of NextGenerationEU, partnership on 'Telecommunications of the Future' (PE00000001—program 'RESTART', Structural Project 'Rigoletto' and Focused Project 'HePIC'). D.A.B.M. acknowledges support by the Air Force Office of Scientific Research (AFOSR, grants FA9550-17-1-0002 and FA9550-21-1-0312). Part of this work was carried out at Polifab, the micro- and nanofabrication facility of Politecnico di Milano (https://www.polifab.polimi.it/). We thank C. De Vita for his support in the realization of the phase masks used in the experiments and V. Grimaldi for his support in the development of the control electronics.

Author contributions

M.M. and S.S. designed the photonic chips and performed the optical measurements. F.Z., G.F. and M. Sampietro developed the electronic control systems. M. Sorel contributed to the design of the photonic chip. S.S., M.M., A.M., D.A.B.M. and F.M. conceived the experiments and analysed the experimental data. S.S., D.A.B.M. and F.M. wrote the manuscript. All the authors contributed to the revision of the manuscript. F.M. supervised the project.

Competing interests

The authors declare no competing interests

Additional information

Extended data is available for this paper at https://doi.org/10.1038/s41566-023-01330-w.

Supplementary information The online version contains supplementary material available at https://doi.org/10.1038/s41566-023-01330-w.

Correspondence and requests for materials should be addressed to Francesco Morichetti.

Peer review information *Nature Photonics* thanks Keren Bergman, Dirk Englund and the other, anonymous, reviewer(s) for their contribution to the peer review of this work.

https://doi.org/10.1038/s41566-023-01330-w

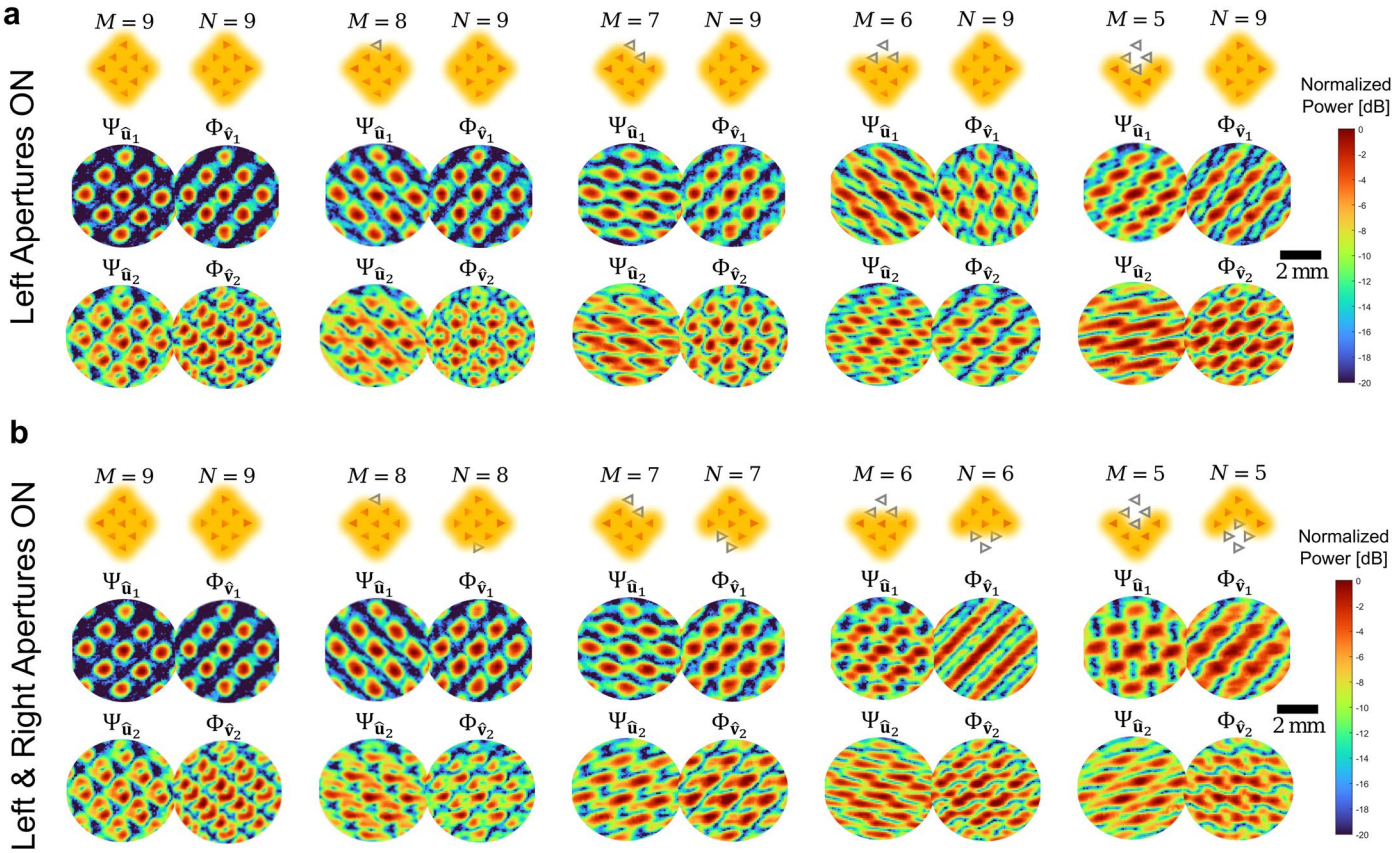

Extended Data Fig. 1 | Beam shapes of orthogonal modes between arbitrary sets of optical apertures. Complete set of beam pairs (far fields $\Psi_{\hat{u}_{1,2}}$ and $\Phi_{\hat{v}_{1,2}}$) measured when the number of input M / output N apertures in the source/receiving volumes are progressively reduced, **a** in a non-symmetric configuration ($M = 9, 8, \ldots, 5; N = 9$), and **b** in a (point-)symmetric configuration ($M = N = 9, 8, \ldots, 5$).

https://doi.org/10.1038/s41566-023-01330-w

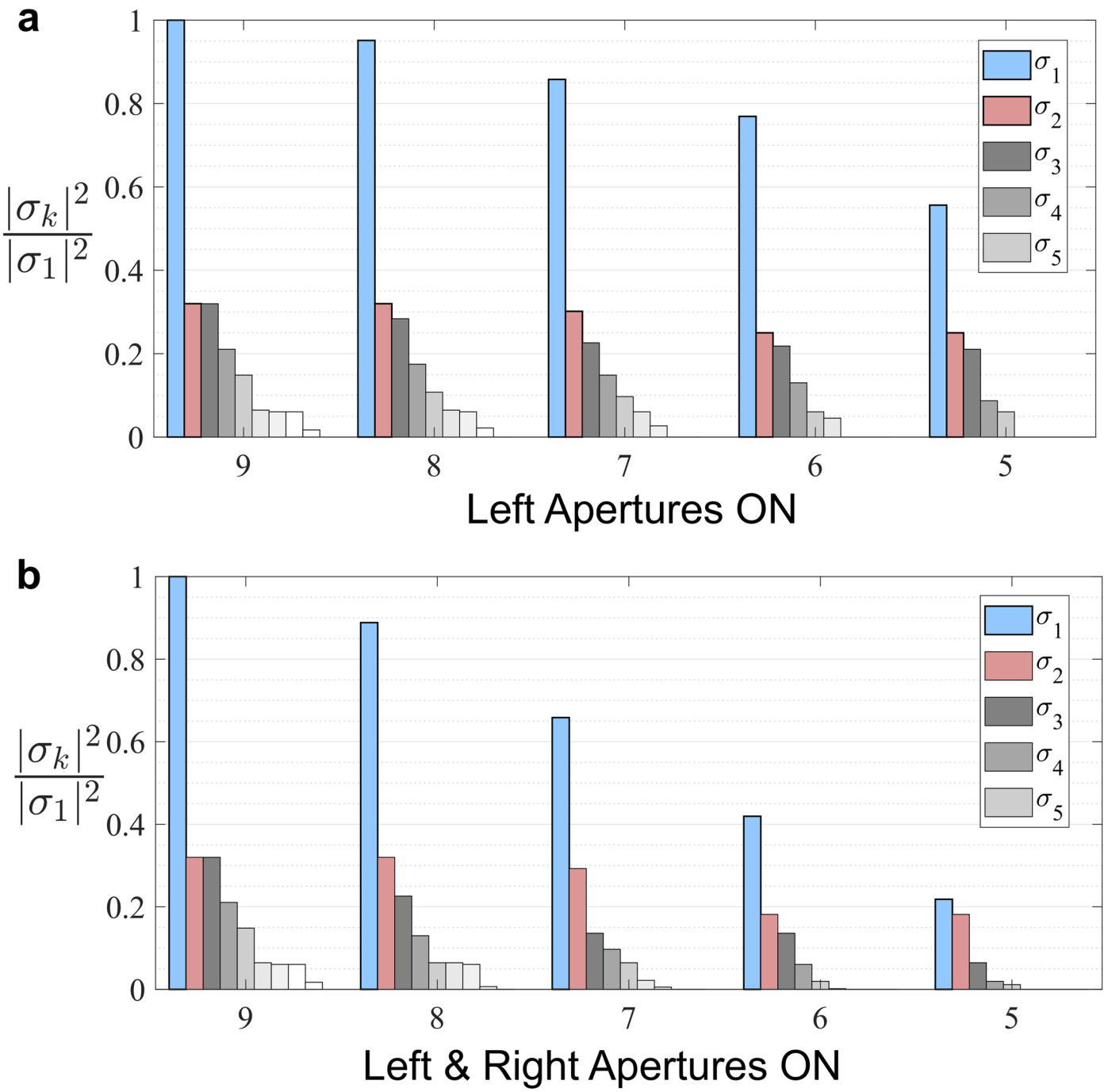

Extended Data Fig. 2 | Coupling strength of mode pairs established between arbitrary sets of optical apertures. Simulated coupling strengths of modes established between the source/receiving volumes when the number of input M and output N apertures are progressively reduced **a** in a non-symmetric configuration ($M = 9, 8, \ldots, 5; N = 9$), and **b** in a (point-)symmetric configuration ($M = N = 9, 8, \ldots, 5$). Coupling strengths are normalized to that of the first mode when $M = N = 9$. Experimental data are shown in Fig. 2b,c, while measured beam shapes are reported in Extended Data Fig. 1.

https://doi.org/10.1038/s41566-023-01330-w

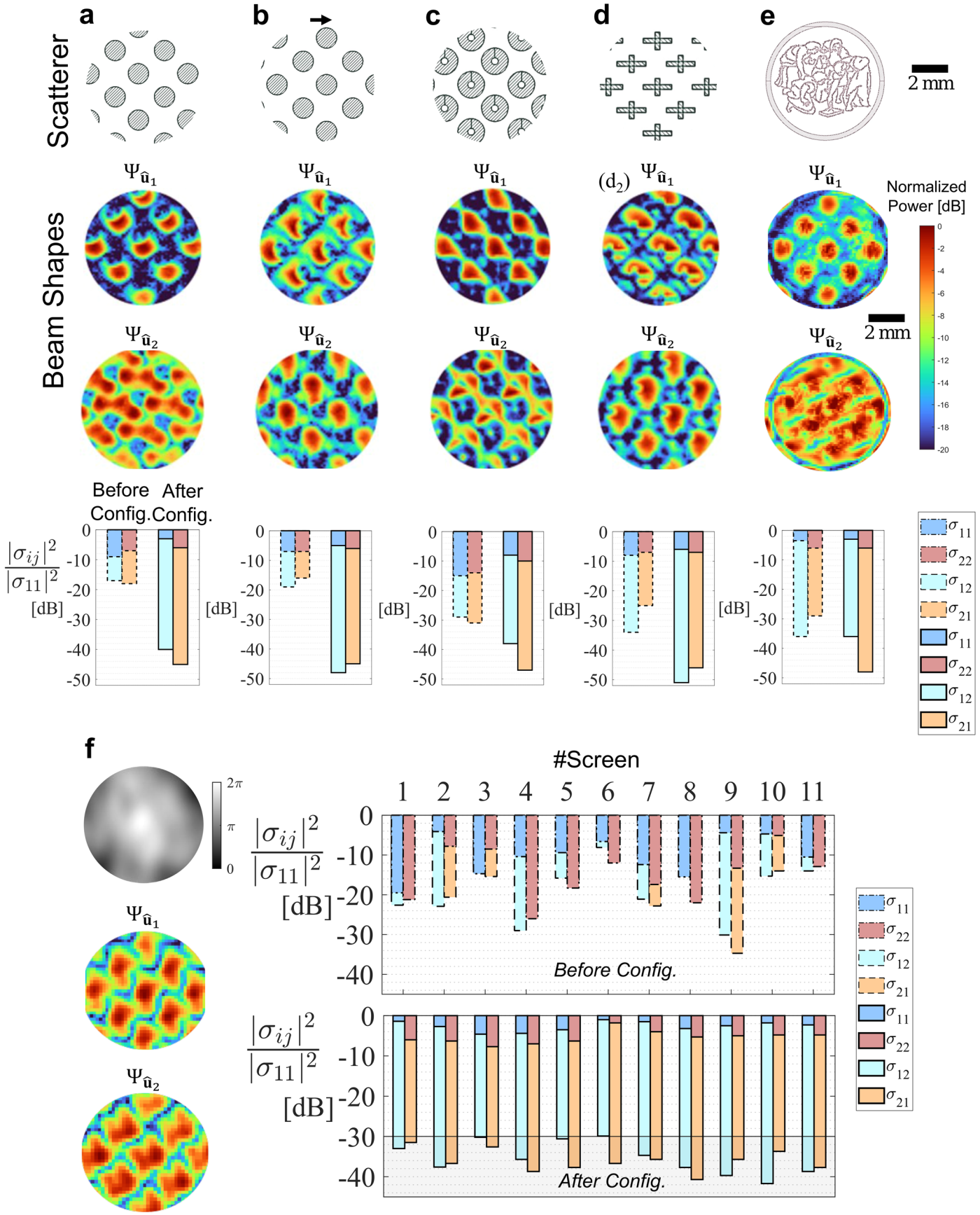

Extended Data Fig. 3 | See next page for caption.

https://doi.org/10.1038/s41566-023-01330-w

Extended Data Fig. 3 | Orthogonal modes through obstacles and scattering media. The full set of obstacles used in the experiments include metal obstructions arranged as a periodic pattern of **a** circles (and laterally shifted in **b**), **c** donuts, **d** crosses, and **e** a microscale reproduction of the Politecnico di Milano logo. The far-field beam shapes of the first two modes $\Psi_{\hat{\mathbf{u}}_{1,2}}$ providing the maximum coupling strengths and the minimum mutual cross-talk through these obstacles are shown. For each case, bar charts show the coupling strength (σ_{ij}, $i=j$) and the mutual cross-talk (σ_{ij}, $i\neq j$), which are both deteriorated with the insertion of the obstacle (dashed bars, before configuration), and can be mostly recovered by optimizing the two photonic processors (solid bars, after configuration). In the experiments reported in panel **f** the obstacle is a phase aberrator emulated by using an SLM; the recovery of the coupling strength (σ_{ij}, $i=j$) and the mutual cross-talk (σ_{ij}, $i\neq j$) is shown for 11 different example configurations of the SLM. The peak-to-peak phase shift introduced by the phase-only aberrator is 2π.